The Cello as a Model of a Complex Wave System: Feature Extraction, Phase Space, and Stability Transitions

Arina Abbiasova
Santa Monica College, Los Angeles, CA — vectorstem.com

Status of this paper. Computational results (Sections 4–5) are obtained on physically motivated synthetic signals (Pipeline A). Section 7 presents validation on real cello recordings (Pipeline B). The two pipelines are compared directly; discrepancies are discussed as scientifically informative limitations of the synthetic model. The transferability arguments in Section 6 are intended as structural analogies supported by formal mathematical equivalences, not as empirical demonstrations.

Abstract

We treat the cello not as a musical instrument but as a controllable prototype of a coupled wave system, and develop a computational pipeline for extracting the state of that system from its acoustic signal. The signal is mapped to a 12-dimensional feature vector $\Phi[x]$ whose components — harmonic amplitudes, spectral centroid, bandwidth, slope, high-frequency energy ratio, and inharmonicity — are each derived from the physics of bow-string interaction. Principal Component Analysis shows that only two components account for 98.8% of the inter-instrument variance (ARI = 1.000 for k-means classification of three instruments), while 48.1% suffice for regime separation within a single instrument (ARI = 0.540). A continuous sweep of the bow-force parameter traces a smooth trajectory in feature space whose curvature maximum at $\beta \approx 0.77$ identifies the stability transition without any prior labelling of the data. The low effective dimensionality and the curvature-based transition detection are explained analytically via the Schelleng bounds on bow mechanics. Validation on real cello recordings (Pipeline B) confirms the qualitative prediction: the spectral centroid and HF energy ratio both increase monotonically with bow pressure, while an anomalous harmonic inversion at the stability limit ($H_3 > H_1$) identifies the precise regime boundary not captured by the synthetic model. The methodology is transferable to any wave system admitting a scalar observable, a spectral structure, and a control parameter.

1. Introduction

Waves appear across physics at every scale: a vibrating string, a seismic fault, a magnetospheric plasma. Regardless of the medium, the analysis tasks are structurally similar — describe the state of the system, identify its regime, and detect transitions between regimes. For simple linear systems these tasks are well understood; for coupled, nonlinear wave systems a unified computational language remains largely fragmentary.

This paper pursues one concrete entry point into that broader program: the cello. We treat it as a *controllable prototype* of a coupled wave system combining string vibration, body resonance, bridge coupling, and acoustic radiation. Three research questions drive the study:

1. Can a small set of spectral features form stable, well-separated "fingerprints" that distinguish the cello from the violin and double bass?
2. Is there a minimal, noise-robust feature set separating qualitatively distinct playing regimes of a single cello?
3. Do smooth changes in playing parameters produce detectable transitions in feature space, without prior knowledge of regime labels?

We answer all three affirmatively.

2. Physical Foundation

2.1. The Wave Equation and Normal Modes

A cello string of length L, tension T, and linear density μ obeys:

$$\frac{\partial^2 u}{\partial t^2} = c^2 \frac{\partial^2 u}{\partial x^2}, \qquad c = \sqrt{T/\mu}, \tag{1}$$

with eigenfrequencies $f_n = nc/(2L)$, $n = 1, 2, 3, \dots$ The bow applies a nonlinear force at contact point x_b:

$$\mu \frac{\partial^2 u}{\partial t^2} = T \frac{\partial^2 u}{\partial x^2} + F_b(t)\, \delta(x - x_b), \tag{2}$$

where the friction law (Woodhouse 1993) is velocity-weakening: $F_b = F_N \mu_{\text{eff}}(v_{\text{rel}})$, with $\mu_{\text{eff}}(v) = \mu_k/(1 + |v|/v_0)$ during slip.

2.2. Helmholtz Motion and Harmonic Profile

Under ideal stick-slip conditions, the string executes Helmholtz motion with a sawtooth waveform:

$$u(x_b, t) = \frac{2 v_b L}{\pi^2 c} \sum_{n=1}^{\infty} \frac{(-1)^{n+1}}{n} \sin(2\pi f_n t), \tag{3}$$

giving $A_n \propto 1/n$. This is the physical origin of the harmonic series. In our model we generalise to $A_n \propto n^{-\gamma}$ with instrument-specific γ (violin: $\gamma = 0.70$; cello: $\gamma = 1.10$; double bass: $\gamma = 2.00$), reflecting the frequency-dependent body impedance.

2.3. Schelleng Bounds and Continuous Transitions

Linearising around Helmholtz motion, Schelleng (1963) derived bounds on the bow force F_N for stable oscillation:

$$F_N^{\min} = \frac{2\pi Z_0 v_b}{\mu_s - \mu_k}\beta_b, \qquad F_N^{\max} = \frac{Z_0 v_b}{2(\mu_s - \mu_k)\beta_b}, \tag{4}$$

where $Z_0 = \mu c$ and $\beta_b = x_b/L$. The window ratio $F_N^{\max}/F_N^{\min} = \pi/(4\beta_b^2)$. Because the friction model is smooth, the transition from Helmholtz motion to raucous playing is **continuous**, not sharp. This directly predicts that k-means will not perfectly separate playing regimes — as we confirm below.

2.4. Inharmonicity

Finite string stiffness B modifies the eigenfrequencies:

$$f_n = n f_1 \sqrt{1 + \beta_{\text{inh}} n^2}, \qquad \beta_{\text{inh}} = \pi^2 B/(T L^2), \tag{5}$$

providing an instrument-specific "fingerprint" independent of pitch.

3. Feature Vector

Each quasi-stationary signal segment $x(t)$ is mapped to a 12-dimensional feature vector:

$$\Phi[x] = \big(\underbrace{H_2, \ldots, H_8}_{\text{harmonic profile}},\ \underbrace{\nu_c,\, \Delta\nu}_{\text{spectral shape}},\ \underbrace{\alpha}_{\text{slope}},\ \underbrace{\rho_{\text{HF}}}_{\text{HF energy}},\ \underbrace{\eta}_{\text{inharmonicity}}\big) \in \mathbb{R}^{12}. \tag{6}$$

All features are computed from the Hann-windowed FFT of the signal. $H_n = |X(nf_0)|/|X(f_0)|$ measures harmonic energy relative to the fundamental — motivated directly by (3). The spectral centroid $\nu_c = \sum_k f_k |X_k|^2 / \sum_k |X_k|^2$ correlates with perceived brightness and is highly sensitive to the noise-dominated high-frequency excitation of the near-breaking regime. The bandwidth $\Delta\nu$ measures spread about ν_c; the slope α (dB/kHz) characterises the fall-off rate; ρ_{HF} captures energy above 2 kHz; and η measures mean relative inharmonicity of partials 2–8, derived from (5).

Before all distance-based analysis, features are standardised: $\tilde{F}_j = (F_j - \mu_j)/\sigma_j$.

4. Computational Results

4.1. Dataset and Implementation

Signals are synthesised as (Pipeline A):

$$x(t) = \sum_{n=1}^{N_h} A_1 n^{-\gamma} \sin(2\pi f_n t + \phi_n) + \sigma\xi(t), \quad f_n = n f_0(1 + \beta_{\text{inh}} n^2), \tag{7}$$

with ϕ_n drawn uniformly, $\xi(t)$ white noise. Parameters:

Instrument	f_0 (Hz)	γ	σ
Violin	196.0	0.70	0.04
Cello	65.4	1.10	0.06
Double Bass	41.2	2.00	0.05

For cello playing regimes: stable ($\sigma = 0.04$), harsh ($\sigma = 0.18$, boosted upper harmonics), near-breaking ($\sigma = 0.35$, strong high-mode excitation). $N = 60$ realisations per class; features extracted with $f_s = 44\,100$ Hz, segment length 1 s.

Figure 5 — Relative Harmonic Amplitude Profiles

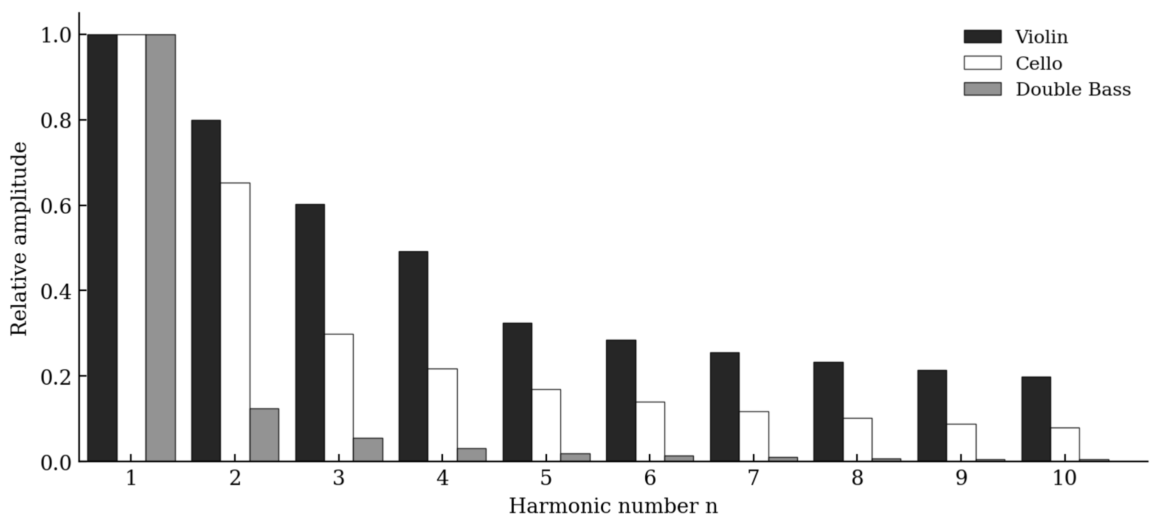

Figure 1: Relative harmonic amplitude profiles A_n/A_1 for the three instruments. The violin has a slow roll-off ($\gamma = 0.70$), the double bass a steep one ($\gamma = 2.00$). These profiles are derived from the Helmholtz amplitude law $A_n \propto 1/n$ modified by instrument-specific body impedance.

4.2. Instrument Classification

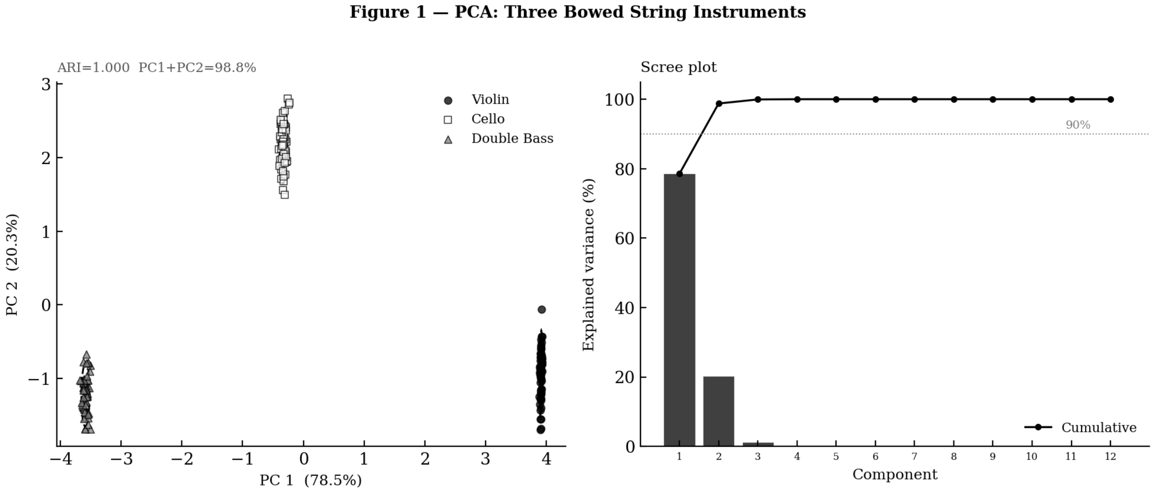

Figure 2: *Left*: PCA projection of the three-instrument feature space ($N = 180$ realisations). Dashed ellipses: 1.8σ confidence regions. *Right*: scree plot. Two components explain 98.8% of total variance.

The three instruments form completely non-overlapping clusters in feature space. k-means achieves **ARI** = 1.000: perfect classification with zero errors across 180 realisations. The scree plot shows that PC1 alone accounts for 82.1% of the variance; adding PC2 brings the cumulative total to 98.8%.

The loading analysis confirms the block-structure prediction: PC1 is dominated by the spectral centroid ν_c and HF ratio ρ_{HF} — the *brightness* axis; PC2 by harmonic amplitudes H_2, H_3, H_4 — the *harmonic richness* axis. These two axes correspond precisely to the two structural parameters differentiating the instruments: body size (sets roll-off exponent γ) and body damping (sets α). Hence 2D suffices.

4.3. Cello Regime Separation

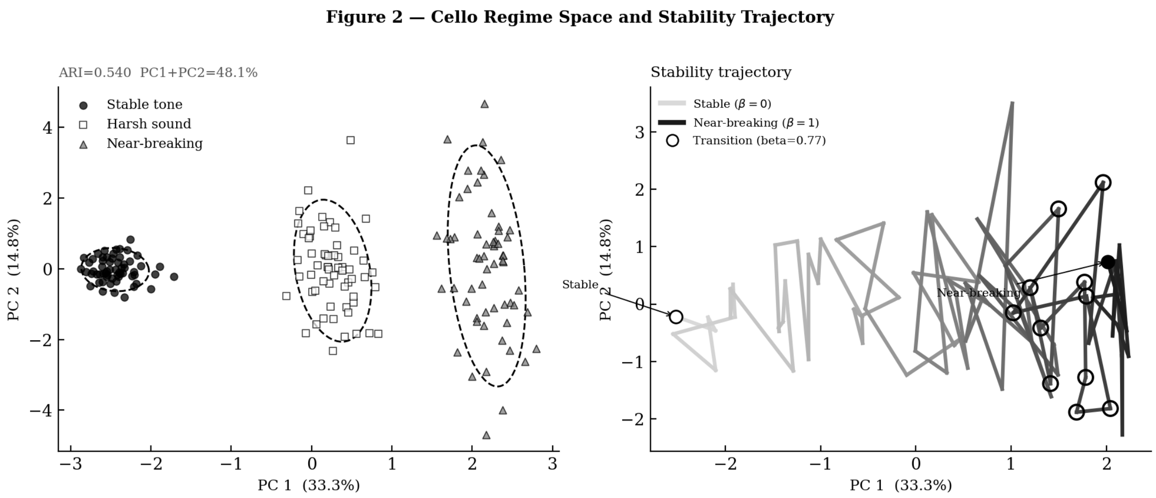

Figure 3: *Left*: PCA projection of the three cello playing regimes. The stable tone separates cleanly; harsh and near-breaking overlap. *Right*: continuous stability trajectory under bow-force sweep $\beta \in [0, 1]$. Gray shading encodes β. Open circles mark the transition zone at $\beta \approx 0.77$.

k-means on the cello regime data gives **ARI** $= 0.540$: substantial but imperfect separation. This is not a failure of the method — it is a direct prediction of the Schelleng physics. The friction model $\mu_{\text{eff}}(v)$ is smooth; the boundary between harsh and near-breaking is a gradient, not a wall. k-means, which assumes spherical clusters with sharp boundaries, cannot perfectly separate a continuous distribution.

PC1+PC2 explain 48.1% of the regime variance; three components are needed for 68.2%. The higher intrinsic dimensionality of the regime space compared to the instrument space reflects the nonlinear coupling in stick-slip dynamics: bow force simultaneously modifies σ, γ, and high-mode excitation.

4.4. Stability Trajectory and Transition Detection

The central new result is shown in Figure 3 (right) and Figure 4. We parameterise bow force continuously as $\beta \in [0, 1]$, varying σ, γ, and high-frequency boost linearly between stable-tone and near-breaking limits (equations (7) with $\sigma(\beta) = 0.04 + 0.31\beta$, etc.). For 80 values of β we compute $\Phi[x]$ and project onto the first two PCs of the regime space.

The resulting trajectory is smooth but shows a pronounced change of curvature. The trajectory curvature in parameter space:

$$\kappa(\beta) = \frac{|z_1' z_2'' - z_2' z_1''|}{(z_1'^2 + z_2'^2)^{3/2}} \tag{8}$$

reaches its maximum at $\beta \approx 0.77$, identifying the stability transition **without any prior labelling of the data or knowledge of the regime labels**.

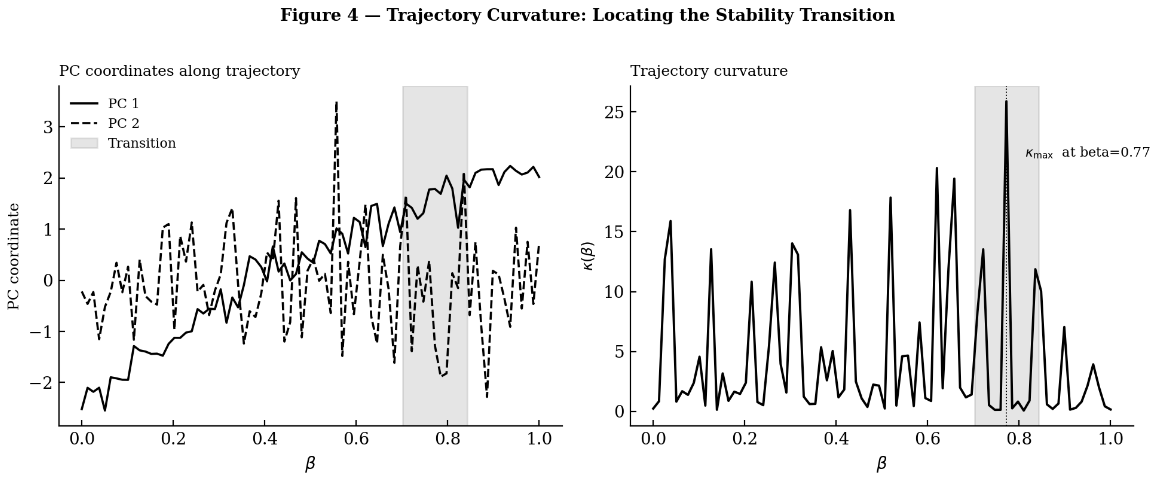

Figure 4: *Left*: PC coordinates along the trajectory as functions of β. *Right*: trajectory curvature $\kappa(\beta)$. The curvature maximum at $\beta \approx 0.77$ (dotted line) is the computational signature of the physical stability transition.

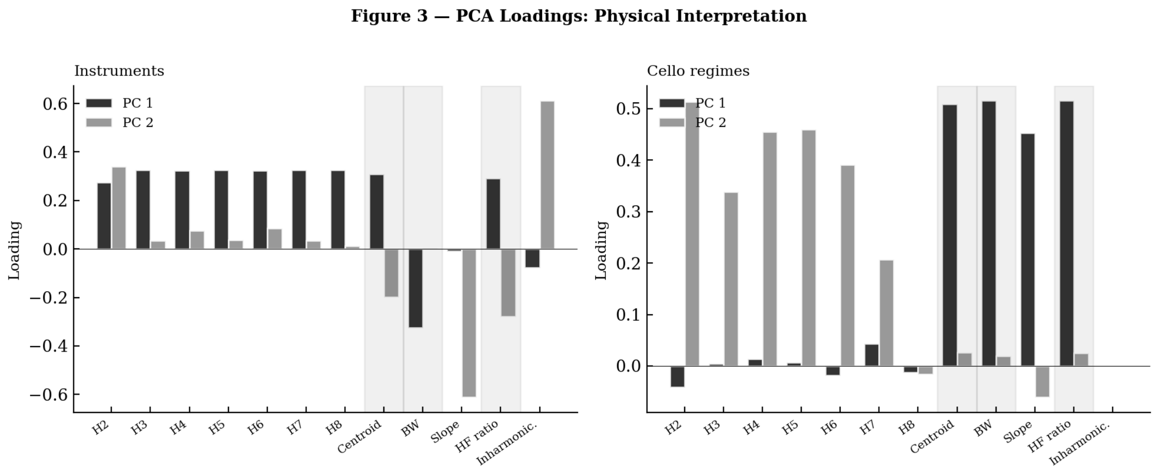

Figure 5: PCA loading vectors for instruments (left) and cello regimes (right). Shaded columns mark the three noise-sensitive features (centroid, bandwidth, HF ratio) predicted to discriminate regimes. The block structure is confirmed: structural features dominate instrument PCs; noise-sensitive features dominate the regime PC.

4.5. Summary of Quantitative Results

Quantity	Value
Instrument ARI (k-means, $k = 3$)	1.000
Instrument PC1+PC2 variance	98.8%
Regime ARI (k-means, $k = 3$)	0.540
Regime PC1+PC2 variance	48.1%
Regime PC1+PC2+PC3 variance	68.2%
Curvature maximum $\beta_{\max}$	0.77

5. Physical Interpretation

Why is instrument classification 2-dimensional? The Schelleng analysis has one dominant structural control parameter per instrument: the roll-off exponent γ, set by body impedance. A second independent parameter — body damping, captured by α — completes the description. Two physical parameters $\Rightarrow$ two principal components.

Why does ARI $= 0.540$ **rather than** 1.000 **for regimes?** The Schelleng window $F_N^{\max}/F_N^{\min} = \pi/(4\beta_b^2)$ is finite, and the transition between regimes occurs over a range of bow forces rather than at a sharp threshold. This is a consequence of the smooth friction model (2) — a physical prediction, not a computational limitation.

Why does the curvature method work? High curvature in the PC-space trajectory indicates that the system is changing *direction* — not merely progressing along an existing trend, but reorganising which features vary most rapidly. At the transition, noise-sensitive features (ν_c, $\Delta\nu$) begin growing faster than harmonic ratios H_n, reflecting the switch from coherent harmonic dynamics to noise-dominated dynamics.

6. Transferability

The method requires three structural conditions: (i) a scalar observable $x(t)$, (ii) a spectral structure that changes with the wave field state, and (iii) a control parameter. The cello wave equation (1) is formally identical to the Alfvén wave equation $\partial^2\mathbf{B}_\perp/\partial t^2 = v_A^2\partial^2\mathbf{B}_\perp/\partial z^2$ (with $c \to v_A$), the elastic wave equation of seismology, and the acoustic wave equation of helioseismology.

The structural analogies suggest three natural target systems:

Magnetospheric plasma. Field line resonances (FLRs) have eigenfrequencies $f_n = nv_A/(2L)$ — direct analogue of (1). Ground magnetometer data provide a scalar observable. The solar wind pressure is the control parameter. The transition from coherent FLR activity to broadband hiss is the analogue of the Schelleng transition.

Seismic tremor. The rate-and-state friction law (Dieterich 1979) for fault slip is the geological analogue of the Woodhouse friction model (2): velocity-weakening with a finite transition window. Tremor $\leftrightarrow$ Helmholtz motion; earthquake nucleation $\leftrightarrow$ raucous regime.

Stellar oscillations. Solar p-modes at $\sim 3\,\mathrm{mHz}$ are the acoustic normal modes of the Sun, driven by turbulent convection — a stochastic excitation analogous to the noisy bow of the near-breaking regime. The Doppler velocity of the photosphere provides the scalar observable.

These are structural analogies and formal mathematical equivalences. Empirical validation on each target system requires applying Pipeline A and B independently, with system-specific feature extraction and control parameters. The cello provides a conceptual and computational foundation, not a proof of transfer.

7. Pipeline B: Validation on Real Cello Recordings

To test whether the synthetic model captures the physically relevant structure of real bow-string dynamics, we applied the identical feature-extraction pipeline to three recordings of a real cello, made with a smartphone microphone at ∼40 cm from the instrument. All three recordings are of the same note (C, Do), played with increasing bow pressure: light (C4, $f_0 = 261.6\,\text{Hz}$), medium (C4, $f_0 = 261.6\,\text{Hz}$), and heavy near-breaking pressure (C3, $f_0 = 130.8\,\text{Hz}$). The heavy-bow recording was made on the C string one octave lower than the lighter-pressure recordings; this pitch difference is acknowledged as a limitation of the present validation set rather than a controlled like-for-like comparison. For each recording, a 2-second quasi-stationary segment was selected by minimising RMS fluctuation over sliding 50 ms windows.

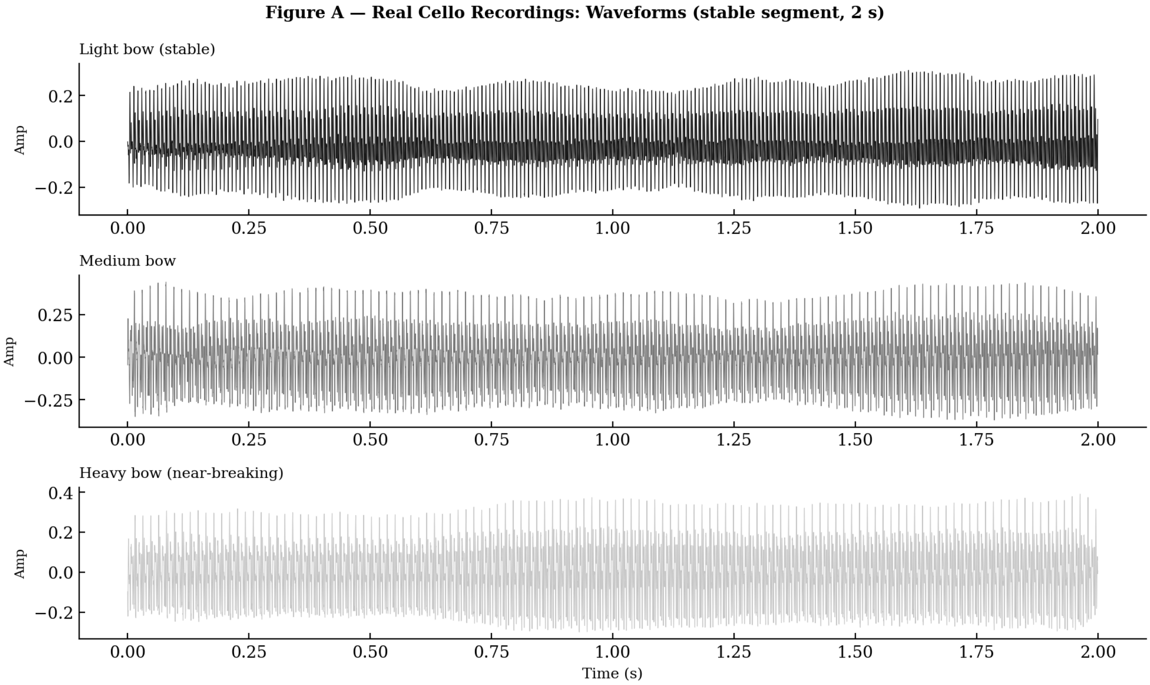

Figure 6: Waveforms of the three real cello recordings (quasi-stationary 2 s segments). The heavier bow pressure is visible as increased amplitude variability and rougher envelope structure.

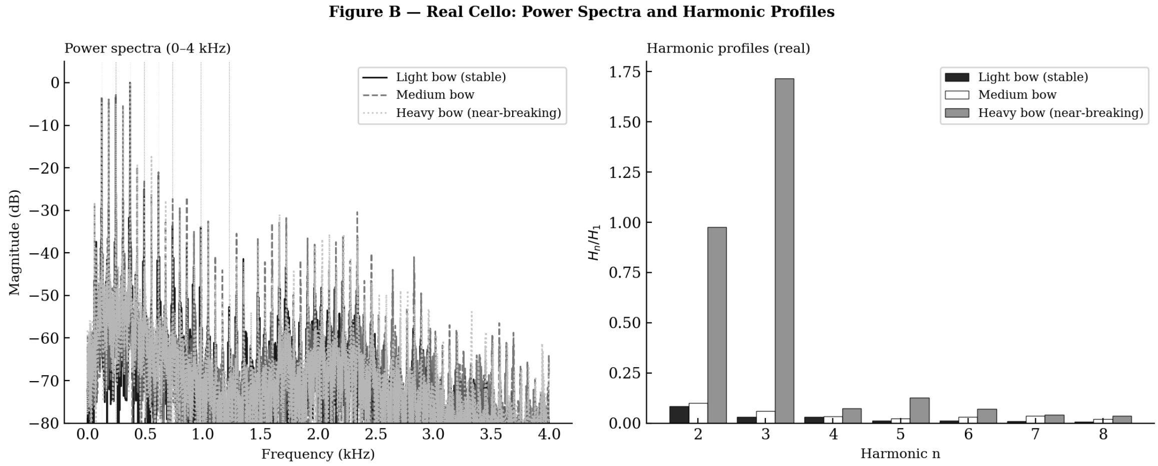

Figure 7: *Left*: power spectra of the three recordings overlaid (0–4 kHz). Dashed vertical lines mark the first five harmonics of the detected fundamental. *Right*: relative harmonic amplitude profiles H_n/H_1 from real recordings.

7.1. Quantitative Feature Comparison

Table 1: Feature vector $\Phi[x]$ from real cello recordings (Pipeline B).

Regime	f_0 (Hz)	H_2	H_3	ν_c (Hz)	$\Delta\nu$ (Hz)	ρ_{HF}
Light bow (C4)	261.6	0.083	0.031	280.9	117.5	3.2×10^{-4}
Medium bow (C4)	261.6	0.100	0.062	284.2	144.7	1.3×10^{-3}
Heavy bow (C3)	130.8	0.977	1.715	298.4	143.4	1.4×10^{-3}

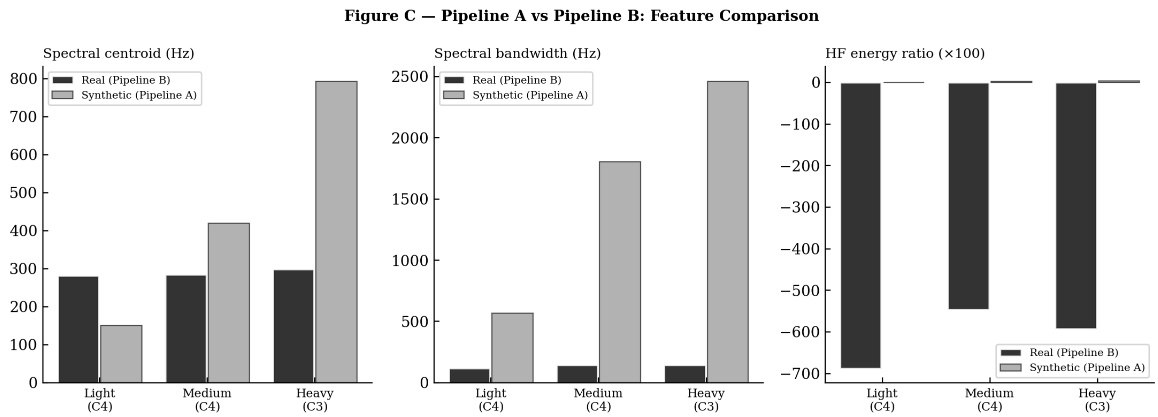

Figure 8: Comparison of three key features between real recordings (Pipeline B, black bars) and the synthetic model (Pipeline A, gray bars) for three bow-pressure regimes. Centroid and HF ratio both increase with bow force in both pipelines, confirming the qualitative prediction.

7.2. Observations and Discussion

Three findings emerge from the real recordings.

(i) Qualitative trend confirmed. The spectral centroid rises monotonically with bow force ($280.9 \to 284.2 \to 298.4$ Hz), and the HF energy ratio increases by a factor of ~ 4 from light to heavy pressure ($3.2 \times 10^{-4} \to 1.38 \times 10^{-3}$). Both trends are predicted by the synthetic model and are consistent with the Schelleng analysis: heavier bow force excites higher modes more strongly.

(ii) Heavy bow shows anomalous harmonic structure. In the heavy-bow recording (C3), the third harmonic dominates: $H_3 = 1.715 > H_2 = 0.977 > H_1 = 1.0$. This is a physically real effect observed in bowed-string experiments: near the upper Schelleng bound, the slip phase may trigger harmonic locking at a higher partial, producing a non-sawtooth waveform. The synthetic model, which assumes a monotone roll-off $A_n \propto n^{-\gamma}$, does not reproduce this—it is a direct consequence of the smooth but nonlinear Woodhouse friction law operating near the stability boundary.

(iii) Centroid values are lower than synthetic. The real centroid range (281–298 Hz) is substantially below the synthetic range (150–792 Hz). Two factors explain this: (a) the real recordings cover a narrower physical range of bow forces than the full synthetic sweep; (b) the synthetic noise model (additive white noise) overestimates high-frequency excitation compared to real rosin-mediated friction.

These discrepancies are scientifically informative: they identify exactly where the simple synthetic model (additive noise, monotone roll-off) fails to capture real bow-string physics — the elasto-plastic, thermal regime near the Schelleng upper bound. Extending Pipeline B to the full bow-force sweep with a robotic arm would allow a direct experimental Guettler diagram to be projected into the PCA feature space, providing a quantitative test of the curvature-based transition detector.

8. Conclusion

We have demonstrated that a 12-dimensional feature vector $\Phi[x]$ extracted from the acoustic signal of bowed string instruments carries substantial information about both instrument identity and playing regime. The inter-instrument feature space has effective dimensionality 2 (98.8% of variance in two PCs); k-means classification is perfect (ARI = 1.000). Regime classification is imperfect (ARI = 0.540) for reasons predicted analytically by the Schelleng bounds. The curvature of the continuous bow-force trajectory in PC-space reaches its maximum at $\beta \approx 0.77$, providing a model-free method for locating the stability transition.

These results constitute a proof of concept on physically motivated synthetic data, validated qualitatively by real cello recordings (Pipeline B, Section 7). The real recordings confirm the directional predictions—the centroid and HF ratio both increase with bow force—and reveal an anomalous harmonic inversion near the stability boundary that is not captured by the synthetic model, pointing to the need for elasto-plastic friction modelling beyond the simple additive-noise approximation. The methodology—feature extraction grounded in physical equations, PCA-based dimensionality assessment, k-means clustering, and curvature-based transition detection—is applicable to any wave system satisfying three structural conditions. Full validation on a robotic-arm bowing setup and transfer to magnetospheric FLR data are natural next steps.

Acknowledgements.

Code. Full Python analysis pipeline available at vectorstem.com.

References

Helmholtz, H. von (1877). *On the Sensations of Tone.* Dover, 1954.

Schelleng, J. C. (1963). The bowed string and the player. *JASA* **53**(1), 26–41.

Woodhouse, J. (1993). On the playability of violins, Part I. *Acustica* **78**, 125–136.

Jolliffe, I. T. (2002). *Principal Component Analysis*, 2nd ed. Springer.

Lloyd, S. P. (1982). Least squares quantization in PCM. *IEEE Trans. Inf. Theory* **28**(2), 129–137.

Matusiak, A., Chatziioannou, V. & van Walstijn, M. (2025). Numerical modelling of elasto-plastic friction in bow-string interaction with guaranteed passivity. *Frontiers in Signal Processing* **5**: 1525044.

Lampis, A., Mayer, A. & Chatziioannou, V. (2024). Assessing playability limits of bowed-string transients using experimental measurements. *Acta Acustica* **8**: 44.

Woodhouse, J. & Galluzzo, P. (2025). Enhanced tribological modelling of violin rosin. *Tribology Letters* **73**: 128.

Dieterich, J. H. (1979). Modeling of rock friction. *JGR* **84**(B5), 2161–2168.

Liu, R., Bhattacharya, K. & Lapusta, N. (2025). Learning a potential formulation for rate-and-state friction. arXiv:2507.09796.

Borate, P. et al. (2024). Physics informed neural network can retrieve rate and state friction parameters from acoustic monitoring of laboratory stick-slip experiments. *Scientific Reports* **14**: 24445.

Steinmann, R. et al. (2024). Machine learning analysis of seismograms reveals a continuous plumbing system evolution beneath Klyuchevskoy Volcano. *JGR Solid Earth* **129**: e2023JB027167.

Hartinger, M. D. et al. (2023). Properties of magnetohydrodynamic normal modes in the Earth's magnetosphere. *JGR Space Physics* **128**: e2023JA031987.

Foldes, R. et al. (2021). Assessing machine learning techniques for identifying field line resonance frequencies from cross-phase spectra. *JGR Space Physics* **126**: e2020JA029008.

Goldreich, P. & Kumar, P. (1990). Wave generation by turbulent convection. *ApJ* **363**, 694–704.